

Achieving desired nodal lines in freely vibrating structures via material-field series-expansion topology optimization

Yi YAN^a, Xiaopeng ZHANG^a, Jiaqi HE^a, Dazhi WANG^b, Yangjun LUO (✉)^c

^a State Key Laboratory of Structural Analysis for Industrial Equipment, Dalian University of Technology, Dalian 116024, China

^b School of Mechanical Engineering, Dalian University of Technology, Dalian 116024, China

^c School of Science, Harbin Institute of Technology, Shenzhen 518055, China

✉ Corresponding author. E-mail: yangjunluo@hit.edu.cn (Yangjun LUO)

© Higher Education Press 2023

ABSTRACT Accurately controlling the nodal lines of vibrating structures with topology optimization is a highly challenging task. The major difficulties in this type of problem include a large number of design variables, the highly nonlinear and multi-peak characteristics of iteration, and the changeable orders of eigenmodes. In this study, an effective material-field series-expansion (MFSE)-based topology optimization design strategy for precisely controlling nodal lines is proposed. Here, two typical optimization targets are established: (1) minimizing the difference between structural nodal lines and their desired positions, and (2) keeping the position of nodal lines within the specified range while optimizing certain dynamic performance. To solve this complex optimization problem, the structural topology of structures is first represented by a few design variables on the basis of the MFSE model. Then, the problems are effectively solved using a sequence Kriging-based optimization algorithm without requiring design sensitivity analysis. The proposed design strategy inherently circumvents various numerical difficulties and can effectively obtain the desired vibration modes and nodal lines. Numerical examples are provided to validate the proposed topology optimization models and the corresponding solution strategy.

KEYWORDS nodal line, topology optimization, structural dynamics design, material-field series-expansion

1 Introduction

Ensuring that precision instruments are working safely and reliably on the main body structure in a vibrating environment is of considerable significance for many real applications, such as aerospace structures and aviation and microelectromechanical systems. An effective method for achieving precise vibration control is to manipulate the shape of structural eigenmodes while considering the desired eigenfrequency value [1–4]. In the adjustment and design of structural eigenmodes and eigenfrequencies, the “nodal line” [5] is considered one of the critical factors. This line is characterized by a series of nodes with zero amplitude in a certain order of eigenmodes, and the appropriate positions of the nodal line can effectively control vibration response and considerably alleviate damage to precision instruments. Therefore, designing and optimizing structures with specific nodal lines are of interest for practical engineering problems, enriching the

dynamic design toolbox with an additional protection mechanism against vibrations.

Topology optimization [6] is currently regarded as a powerful design tool for improving structural performance. In the past 30 years, topology optimization methods, such as density-based method [7,8], evolutionary structural optimization method [9,10], level-set method [11,12], and phase-field method [13], have been successfully applied to structural dynamic design problems. Existing studies have focused on single or multiple eigenfrequency indexes, such as maximizing natural frequency [14–17] or obtaining the desired eigenfrequencies of certain orders [18,19], minimizing dynamic compliance [17,19–22], and maximizing frequency bandgap [23–25]. Suppressing or utilizing structural resonance caused by external excitation is typically a major concern, and it has been comprehensively studied in eigenfrequency optimization problems. Meanwhile, specified eigenmode designs with topology optimization methods have also been investigated further. For example, setting the maximization of the vibration

amplitude of a planar mechanism as the objective function, Tcherniak [26] derived the modal sensitivity involved in the modal superposition method. Nishiwaki et al. [27] and Maeda et al. [28] proposed a topological design method for vibrating structures with specified eigenfrequencies and portions of specified eigenmode shapes by adopting a multi-objective function that comprehensively balances eigenfrequencies, eigenmode shapes, and stiffness. Tsai and Cheng [29] introduced a modal assurance criterion into structural topology optimization for maximizing the fundamental frequency and obtaining user-defined vibration modes. Xue et al. [30] studied an improved bidirectional evolutionary structural optimization method to achieve modal control and vibration suppression by minimizing amplitudes at specific points. With the superior dynamic properties obtained using topological optimization tools, new conceptual configurations have been proposed for the design of piezoelectric transducers [31–33], actuators, and microplate resonators [34,35]. For most existing methods, local or global approximation to the desired mode shapes can be achieved by controlling eigenmode amplitudes at certain points in the structures. However, strict control of the nodal lines is not guaranteed.

Strictly controlling the shapes and positions of nodal lines is highly significant for the structural optimization design problems of some devices. Relevant studies have confirmed that in the flutter mechanism of wings [36,37] and solar sails [38], the nodal lines of each flutter dangerous mode exert a considerable influence on it; in rail transit, the nodal lines of the body should also be designed within the specified areas to improve safety and passenger comfort [39,40]. In addition, precision instruments and attitude sensors are placed on nodal lines as much as possible in various mechanisms, such as those in rocket engines, space telescopes, and satellite solar panels. Some researchers have attempted to solve this problem by considering predefined orders of eigenmodes on the basis of gradient-based topology optimization methods. For example, Xiang et al. [36] established the display relationship between the positions of nodal lines and design parameters. They obtained the desired nodal lines of a certain wing model by minimizing the area enclosed by the current and desired node lines. Yu et al. [5] performed thickness optimization by minimizing the amplitude of some specific points in predetermined order modes; they obtained the desired nodal lines for the second- and fifth-order eigenmodes of a violin top plate. Mao et al. [41] introduced the node line position constraint of predefined order eigenmodes into the eigenfrequency topology optimization problem and solved it by using an evolutionary structural optimization method. Existing optimization methods can be used to achieve the desired nodal line of order-predefined eigenmodes, in which sensitivity can be derived on the basis of order-predefined eigenmode sensitivity analysis

methods [26,36]. However, when the modal orders of eigenmodes switch during structural optimization or when modal shapes cannot be specified in advance, solving optimization problems with the existing gradient-based optimization algorithm becomes extremely difficult. Moreover, some numerical issues, such as localized eigenmodes [15,24,26], eigenmode order switching [20,42], and the nonexistence of the derivative for repeated eigenvalues [23,24], also increase the difficulty of solving dynamic optimization problems. Although some aggregation techniques have been developed to address these challenges, the high nonlinearity of the objective or constraint functions also makes obtaining satisfactory results difficult for the optimization problem when considering nodal lines and frequencies.

As early as 1993, Grandhi [1] pointed out that gradient-free algorithms, such as neural networks and genetic algorithms, can be used to solve dynamic topology optimization problems. Recently, Luo et al. [43] provided a new gradient-free topology optimization method that combines the material-field series-expansion (MFSE) method and the sequential Kriging surrogate model (KG). The resulting KG-MFSE method has been successfully used in the bandgap maximization design of photonic and phononic crystals [44–46].

In the current study, we propose MFSE-based topology optimization models for achieving desired nodal lines in vibrating structures. Without introducing prespecified eigenmode order requirements or additional eigenmode order switching treatment techniques, two types of topology optimization models are proposed. The first one minimizes the difference between structural nodal lines and their desired positions, and the second one optimizes certain performance while keeping the position of the nodal lines within the specified range. With the MFSE method [47], structural topology can be decoupled from the finite element mesh and sufficiently represented by a small number of design variables. Therefore, we can freely refine the finite element mesh to obtain more accurate nodal lines and solve optimization problems without increasing the number of design variables and iteration steps. Here, the sequential Kriging-based optimization algorithm [43] that does not require design sensitivity information is adopted as the optimizer. With the proposed optimization method, the potential mode switching problem can be easily overcome and desired nodal lines at undefined-ordered eigenmodes can be obtained after optimization.

2 Identification of eigenmode nodal lines

For a freely vibrating structure without any external excitation, the linear motion equation can be given in the finite element form as

$$M\ddot{\mathbf{u}} + \mathbf{K}\mathbf{u} = 0, \quad (1)$$

where \mathbf{K} and \mathbf{M} denote the structural stiffness and mass matrices, respectively, and \mathbf{u} and $\ddot{\mathbf{u}}$ are the vectors of the degrees of freedom and accelerations, respectively. For freely vibrating systems, the generalized eigenvalue problem typically reads as

$$(\mathbf{K} - \lambda_m \mathbf{M}) \Phi_m = 0, \quad m = 1, 2, \dots, \quad (2)$$

where the m th eigenvalue $\lambda_m = \omega_m^2$, ω_m is the m th eigenfrequency, and Φ_m is the corresponding eigenmode.

With the obtained eigenpair solutions of Eq. (2), the eigenmode nodal lines can be identified by interpolating a certain eigenmode contour field. Figure 1(a) shows the contour of the m th eigenmode for a rectangular freely vibrating flat plate (the left edge is fixed), in which the gray areas represent the regions with an extremely small eigenmode amplitude. The corresponding nodal lines L_m extracted from the zero-value lines in the m th eigenmode is shown in Fig. 1(b), i.e., $\Phi_m(\mathbf{r} \in L_m) = 0$, where \mathbf{r} is the coordinate vector. In the numerical implementation, the continuous nodal lines can be approximately discretized by a series of points, which are represented by red circles in Fig. 1(b). In general, the nodes on the nodal lines do not coincide with the finite element mesh but their coordinates can be easily determined via piecewise polynomial interpolation on Φ_m .

3 Topology optimization models of freely vibrating structures that consider desired nodal lines

The topological design of frequency and nodal line optimization problems can be defined as follows: to maximize (or minimize) a certain frequency-dependent performance function while (1) causing the nodal lines to have desired positions and shapes, or (2) constraining the nodal lines within a specified range. In both problems, frequency orders that correspond to the desired nodal lines are difficult to predestine and “mode switching” may occur during optimization. In this regard, a total of

M (M is sufficiently large) orders of eigenfrequencies and the corresponding eigenmodes are calculated and incorporated into the optimization models. As shown in Fig. 2, assume that an eigenmode has K desired nodal lines (denoted by $L_1^*, L_2^*, \dots, L_K^*$), whose order is unknown. For the m_q th order eigenmode ($m_q = 1, 2, \dots, M$), the corresponding nodal lines can be identified and the number of current nodal lines is denoted by K' . If $K' = K$, then the difference between the desired nodal lines L_k^* ($k = 1, 2, \dots, K$) and the current nodal lines L_{k,m_q} ($k = 1, 2, \dots, K$) is quantified as the sum of the distances between corresponding nodes. The nodal line measurement function f_{m_q} for the m_q th eigenmode is defined as

$$f_{m_q} = \begin{cases} \sum_{k=1}^K \sum_{j=1}^{N_p} (\|\mathbf{r}_{k,j}^* - \mathbf{r}_{k,j,m_q}\|_2), & \text{if } K = K', \\ 10^6, & \text{if } K \neq K', \end{cases} \quad m_q = 1, 2, \dots, M, \quad (3)$$

where $\|\cdot\|_2$ denotes the 2-norm. For simplicity, the desired nodal line L_k^* and the current nodal line L_{k,m_q} are discretized into N_p nodes, denoted by $\mathbf{r}_{k,j}^*$ and \mathbf{r}_{k,j,m_q} ($k = 1, 2, \dots, K; j = 1, 2, \dots, N_p$), respectively.

For the first type of nodal line optimization problem, the topology optimization model is described as finding the optimal material distribution of structures that achieves the desired nodal lines and frequency requirements; that is, optimization model 1:

$$\min_{\chi(\mathbf{r})} C_1 = \min \{\ln(f_1), \ln(f_2), \dots, \ln(f_M)\} + \zeta(\omega_i), \quad (4)$$

where $\chi(\mathbf{r}) \in \{-1, 1\}$ represents the structural topology in the design domain Ω_{des} and $\zeta(\omega_i)$ ($i = 1, 2, \dots, M$) is a user-specified function for some specific order eigenfrequencies.

For the second type of nodal line optimization problem, the objective is to maximize (or minimize) certain performance function while keeping the position of the nodal lines within the specified range. In such case, for the m_q th order eigenmode, a constraint function g_{m_q} for judging the nodal line position is defined as

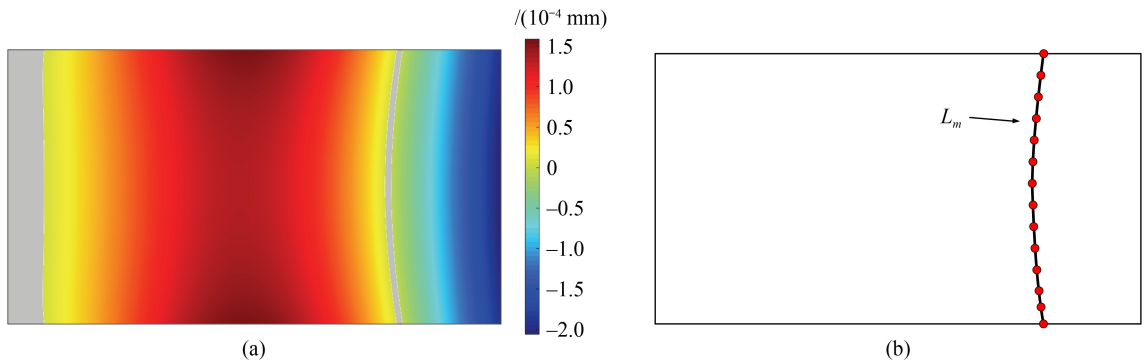


Fig. 1 Schematic of (a) the m th eigenmode contour and (b) evenly distributed points on the nodal line.

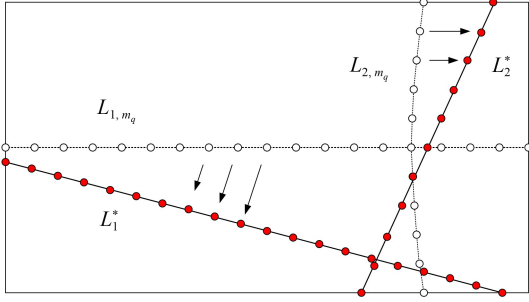


Fig. 2 Comparison of the desired and current nodal lines. The red circles and solid lines represent the desired nodes and nodal lines, respectively. The white circles and dashed lines represent the current nodes and nodal lines, respectively.

$$g_{m_q} = \begin{cases} \sum_{k=1}^K \sum_{j=1}^{N_p} (\max\{0, \|\mathbf{r}_{k,j,m_q} - \mathbf{r}_{k,j}^*\|_2 - \Delta_j\}), & \text{if } K = K', \\ 10^6, & \text{if } K \neq K', \end{cases}$$

$$m_q = 1, 2, \dots, M, \quad (5)$$

where Δ_j is the allowable deviation of the current nodal lines from the desired nodal lines.

Then, the topology optimization model can be formulated to minimize the user-specified frequency function that considers the position constraints of the nodal lines, i.e., optimization model 2:

$$\begin{aligned} \min_{\chi(\mathbf{r})} C_2 &= \zeta(\omega_i), \\ \text{s.t. } G &= \min\{g_1, g_2, \dots, g_M\} \leq 0. \end{aligned} \quad (6)$$

For aforementioned optimization models, the order of the eigenmode with the most desired nodal lines is determined during the optimization procedure by $\min\{\ln(f_1), \ln(f_2), \dots, \ln(f_M)\}$ or $\min\{g_1, g_2, \dots, g_M\}$. Notably, by using the linear weighting approach, the optimization models in Eqs. (4) and (6) can be easily extended to deal with optimization problems with the requirement of nodal lines that consider multiple eigenmodes.

4 Optimization solution strategy

The two types of optimization models shown in Eqs. (4) and (6) involve the switch trap of eigenmode orders and discontinuous objective functions during topology optimization, and thus, they are difficult to solve directly by using conventional gradient-based approaches. Although some techniques, such as approximate aggregation functions [48,49] and mode-tracking methods [20,42], may be applicable, the optimization solution will be extremely unstable due to its highly nonlinear and multi-peak characteristics. In the current study, we adopted an MFSE-based gradient-free framework [43] to solve topology optimization problems that concerned nodal lines and frequencies. First, this framework represents structural topology with a few design variables. Then, it

employs a self-adaptive Kriging-based optimization algorithm to solve the optimization problem effectively without performing sensitivity analysis.

4.1 Topological description based on MFSE

In the MFSE model [47], structure topology is described by a continuous material-field function $\varphi(\mathbf{r}) \in [-1, 1]$, where $\mathbf{r} \in \Omega_{\text{des}}$ is the coordinate vector in the design domain, $\varphi(\mathbf{r}) = -1$ represents the void regions, and $\varphi(\mathbf{r}) = 1$ represents the solid regions. Heaviside function projection is used to map the structural topology and material-field function, namely,

$$\chi(\mathbf{r}) = \begin{cases} \varphi(\mathbf{r}) \cdot e^{-\beta} + 1 - e^{-\beta\varphi(\mathbf{r})}, & \text{if } \varphi(\mathbf{r}) \geq 0, \\ \varphi(\mathbf{r}) \cdot e^{-\beta} - 1 + e^{\beta\varphi(\mathbf{r})}, & \text{if } \varphi(\mathbf{r}) < 0, \end{cases} \quad (7)$$

where β is a parameter that controls the smoothness of the mapping.

With the rational approximation of material property (RAMP) model [50] for material interpolation, the Young's modulus E and mass density ρ in the design domain are expressed by

$$\begin{aligned} E(\mathbf{r}) &= E_{\min} + \frac{1 + \chi(\mathbf{r})}{2 + p(1 - \chi(\mathbf{r}))} (E_0 - E_{\min}), \\ \rho(\mathbf{r}) &= \rho_{\min} + (\rho_0 - \rho_{\min}) \frac{1 + \chi(\mathbf{r})}{2}, \end{aligned} \quad (8)$$

where E_0 and ρ_0 are the Young's modulus and mass density of the considered solid material, respectively, E_{\min} and ρ_{\min} are the small values for avoiding single-element matrices, and the penalty parameter is typically set as $p = 4$.

Here, the material-field function $\varphi(\mathbf{r})$ is constructed with a certain spatial dependence defined by the relationship $C(\mathbf{r}_i, \mathbf{r}_j) = \exp(-\|\mathbf{r}_i - \mathbf{r}_j\|^2 / l_c^2)$, where l_c is the given correlation length that represents topology complexity [47]. In the numerical implementation, the design domain is discretized into N_{MFP} uniformly distributed material points \mathbf{r}_i ($i = 1, 2, \dots, N_{\text{MFP}}$), and a so-called correlation matrix \mathbf{C} is expressed as

$$\mathbf{C} = \begin{Bmatrix} 1 & C(\mathbf{r}_1, \mathbf{r}_2) & \cdots & C(\mathbf{r}_1, \mathbf{r}_{N_{\text{MFP}}}) \\ C(\mathbf{r}_2, \mathbf{r}_1) & 1 & \cdots & C(\mathbf{r}_2, \mathbf{r}_{N_{\text{MFP}}}) \\ \vdots & \vdots & \ddots & \vdots \\ C(\mathbf{r}_{N_{\text{MFP}}}, \mathbf{r}_1) & C(\mathbf{r}_{N_{\text{MFP}}}, \mathbf{r}_2) & \cdots & 1 \end{Bmatrix}, \quad (9)$$

where \mathbf{C} is an $(N_{\text{MFP}} \times N_{\text{MFP}})$ -dimensional, symmetric positive-definite real matrix.

In accordance with bounded field theory [51], the material-field function $\varphi(\mathbf{r})$ is approximately expressed as a linear superposition based on the eigenpairs of \mathbf{C} , i.e.,

$$\varphi(\mathbf{r}) \approx \boldsymbol{\eta}^T \boldsymbol{\Lambda}^{-1/2} \boldsymbol{\Phi}^T \mathbf{C}_d(\mathbf{r}), \quad (10)$$

where $\boldsymbol{\eta} = \{\eta_1, \eta_2, \dots, \eta_N\}^T$ is the vector of the undetermined coefficients or design variables, $\boldsymbol{\Lambda} = \text{diag}(\lambda_1, \lambda_2, \dots, \lambda_N)$ and $\boldsymbol{\Phi} = \{\psi_1, \psi_2, \dots, \psi_N\}$ are the diagonal matrix composed of

the first N largest eigenvalues and the corresponding eigenvectors, respectively, and $C_d(\mathbf{r})$ denotes the vector $\{C(\mathbf{r}, \mathbf{r}_1), C(\mathbf{r}, \mathbf{r}_2), \dots, C(\mathbf{r}, \mathbf{r}_{N_{\text{MFP}}})\}^T$. In general, the dimensionality of the space of $\boldsymbol{\eta}$ for representing the material field is small compared with the number of material points N_{MFP} .

4.2 Solution aspect

After using a small number of design variables $\boldsymbol{\eta}$ to describe structural topology, the sequential Kriging-based optimization algorithm in Ref. [43] is employed to solve the optimization problems in Eqs. (4) and (6). In the gradient-free solution, in accordance with an adaptive design-domain adjusting technique, the optimization problem is reformulated into a series of suboptimization problems that use Latin hypercube sampling to construct Kriging surrogate models and then update the design variables on the basis of the sampling criterion. After the previous suboptimization problem is solved, the optimization strategy will adjust the position of the next suboptimization problem in accordance with the optimization results, and then gradually reduce its range to improve the accuracy of the Kriging surrogate models by increasing the density of samples. In general, 12–15 suboptimization problems must be solved to find the optimal solution. For all the optimization problems in this study, we set the sample center of the initial suboptimization problem at $\boldsymbol{\eta}_c = 0$, and the corresponding design space is denoted by $\Omega_0 = \{\|\boldsymbol{\eta} - \boldsymbol{\eta}_c\|_\infty \leq 0.2\}$. During practical optimization, the smooth parameter β in Eq. (7) will be gradually increased from 0 to 300 as suboptimization problems progress. For details about the sequential Kriging-based optimization algorithm, refer to Ref. [43].

5 Numerical applications and discussion

5.1 Nodal line optimization of a bi-material cantilever plate

We first consider the nodal line optimization of a bi-material cantilever plate. As shown in Fig. 3(a), a bi-material plate is fixed on the left side with a thickness of 0.5 mm, and its length and width are 180 mm, respectively. The properties of Material 1 are as follows: Young's modulus $E_1 = 210$ GPa, Poisson's ratio $\mu_1 = 0.3$, and mass density $\rho_1 = 7850$ kg/m³. Meanwhile, the properties of Material 2 are as follows: $E_2 = 21$ GPa, $\mu_2 = 0.3$, and $\rho_2 = 785$ kg/m³. In the optimization design problem, the plate is divided into 180×100 finite elements, and the design domain is equally distributed by $N_{\text{MFP}} = 90 \times 50$ observation points. The correlation length of the material field is set as $l_c = 100 \times 0.25 = 25$ mm. With the MFSE model, the structure topology can be

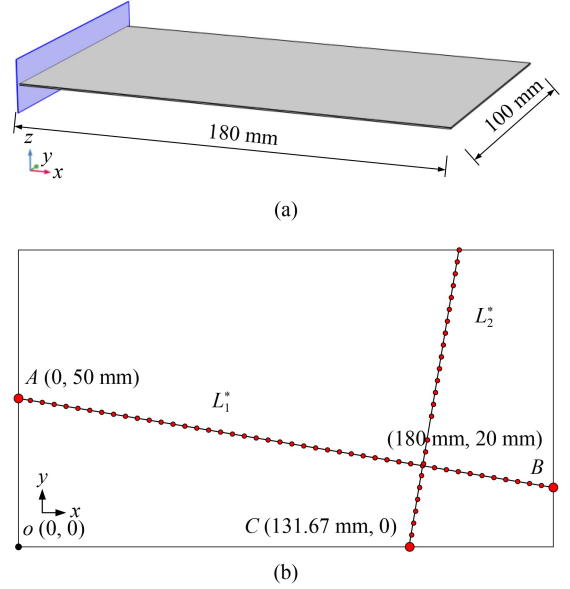


Fig. 3 Bi-material cantilever plate: (a) design domain and (b) two desired nodal lines.

represented by only $N = 63$ independent design variables.

The desired shapes and positions of two nodal lines, denoted by L_1^* and L_2^* (the superscript * represents the desired value), are shown in Fig. 3(b). With point O at the lower left corner of this plate as the coordinate origin, L_1^* is the straight line passing through point A (0 mm, 50 mm) and point B (180 mm, 20 mm), and it is represented by 46 uniformly distributed nodes in the numerical implement. The nodal line L_2^* , represented by 51 uniformly distributed nodes, passes point C (131.67 mm, 0 mm) and is perpendicular to L_1^* .

In this example, optimization model 1 proposed in Eq. (4) is adopted. Considering that the desired nodal lines L_1^* and L_2^* belong to two separate eigenmodes, three design requirements, denoted as Cases 1–3, are tested to demonstrate the ability of the present framework to control nodal lines.

In Case 1, the optimization problem is defined as maximizing the first-order eigenfrequency while obtaining a nodal line closest to the first desired nodal line L_1^* . The objective function of this multi-objective optimization can be reformulated as $\min C = \alpha \ln(\min\{f_1, f_2, \dots, f_M\}) - (1 - \alpha)\omega_1$, where α is a weighting factor (0.5 in this case). As shown in Fig. 4, with the sequential sampling and updating of 12 suboptimization problems, the optimization procedure converges after 2846 finite element calculations. During sampling, the values of samples change significantly. The objective function also exhibits a steady decline in updating the design variables. Furthermore, the values of the samples are gradually decreased as the suboptimization problem progresses due to the decreasing suboptimization space, and they converge to stability since the 8th suboptimization problem. The optimization algorithm determines that the

designed nodal line belongs to the second-order eigenmode of the plate, and the optimized topology and corresponding nodal line are illustrated in Fig. 5. In Fig. 5(a), the red region denotes Material 1, and the blue region denotes the weaker Material 2. Notably, for the plate structure composed entirely of Material 1, the first-order eigenfrequency is $\omega_1 = 13.26$ Hz. The first-order eigenfrequency of the optimized structure increases from $\omega_1 = 13.26$ Hz to $\omega_1^* = 21.51$ Hz. Figures 5(b) and 5(c) show the contour for the first and second eigenmodes of the optimized structure, respectively, and the gray region represents the area where the eigenmode amplitude is extremely small. A comparison between the optimized

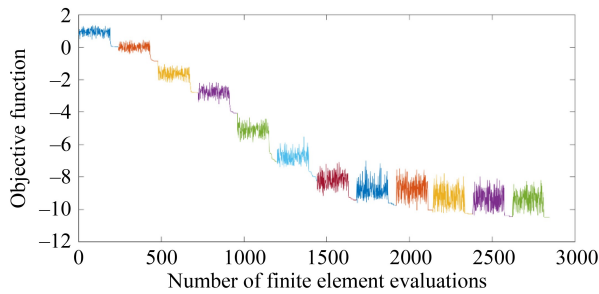


Fig. 4 Topology optimization history of the bi-material cantilever plate that considers the desired nodal lines in Case 1. Different colors represent different suboptimization problems, with 12 suboptimization problems and 2846 finite element calculations.

nodal line L_1 and the desired one L_1^* is presented in Fig. 5(d), which exhibits good agreement in terms of shape and position. From the discrete 41 nodes on the nodal line, the average position deviation between the optimized nodal line and the corresponding desired one is 0.162 mm, and the maximum position deviation is $\max(\|r_{1,j}^* - r_{1,j}\|_2) = 0.522$ mm, which is extremely small compared with the size of the whole plate structure.

In Case 2, we only consider the optimization design for the second desired nodal line L_2^* and simultaneously satisfy the specified first-order eigenfrequency $\omega_1^* = 15$ Hz. The objective function in Eq. (4) can be reformulated as $\min C = \ln(\min\{f_1, f_2, \dots, f_M\}) - p \cdot |\omega_1 - \omega_1^*|$ (here, the penalty factor $p = 10$). The optimized topology and corresponding eigenmode contours are illustrated in Fig. 6. In this case, the obtained nodal line L_2 in the third-order eigenmode of the optimized plate structure is extremely close to the desired nodal line L_2^* . The average position error between the optimized and desired nodal lines is only 0.1214 mm. As shown in Fig. 6, the topology of the structure is considerably changed from Case 1, and the first-order eigenfrequency is $\omega_1^* = 15.00$ Hz, which is strictly controlled at the desired frequency value with nearly no error.

In Case 3, we consider the design requirements of maximizing the first-order frequency and satisfying the two desired nodal lines L_1^* and L_2^* simultaneously. On the basis of the nodal line topology optimization mode in

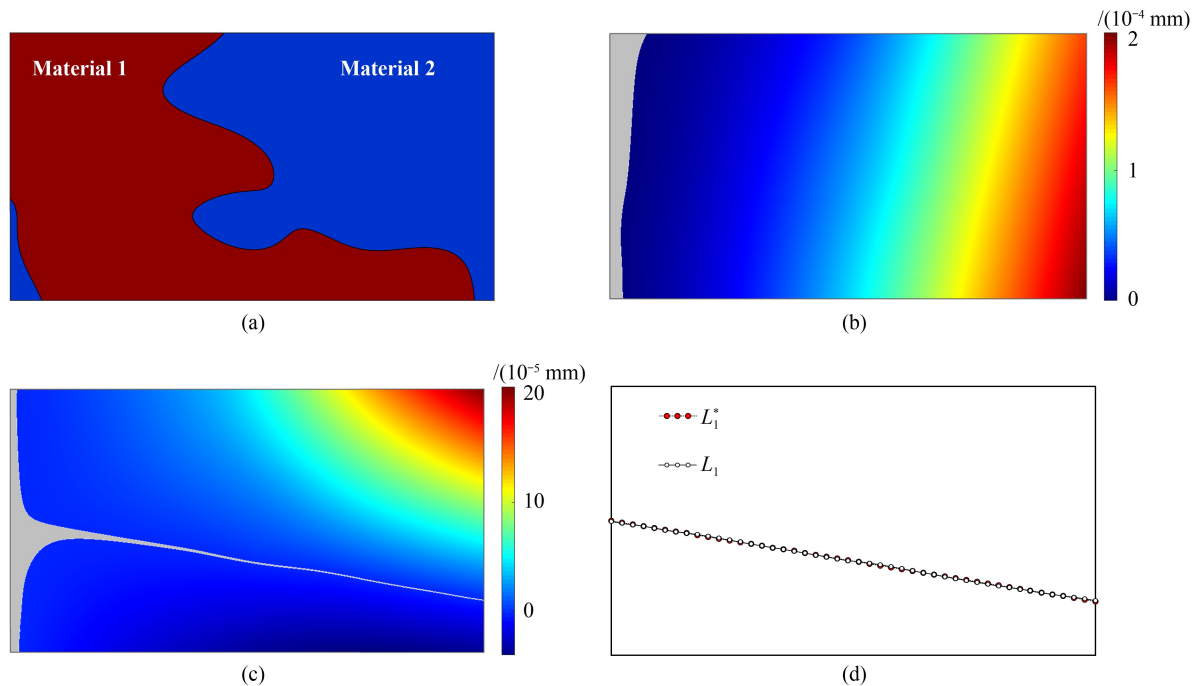


Fig. 5 Optimized solution for achieving the first desired nodal line in Case 1: (a) structural topology. The red region denotes Material 1, while the blue region denotes the weaker Material 2. Contour for (b) the first-order eigenmode with $\omega_1^* = 21.51$ Hz and (c) the second-order eigenmode. The gray region represents the area where amplitude is extremely small. (d) Comparison between the desired nodal line L_1^* and the optimized nodal line L_1 of the second-order eigenmode.

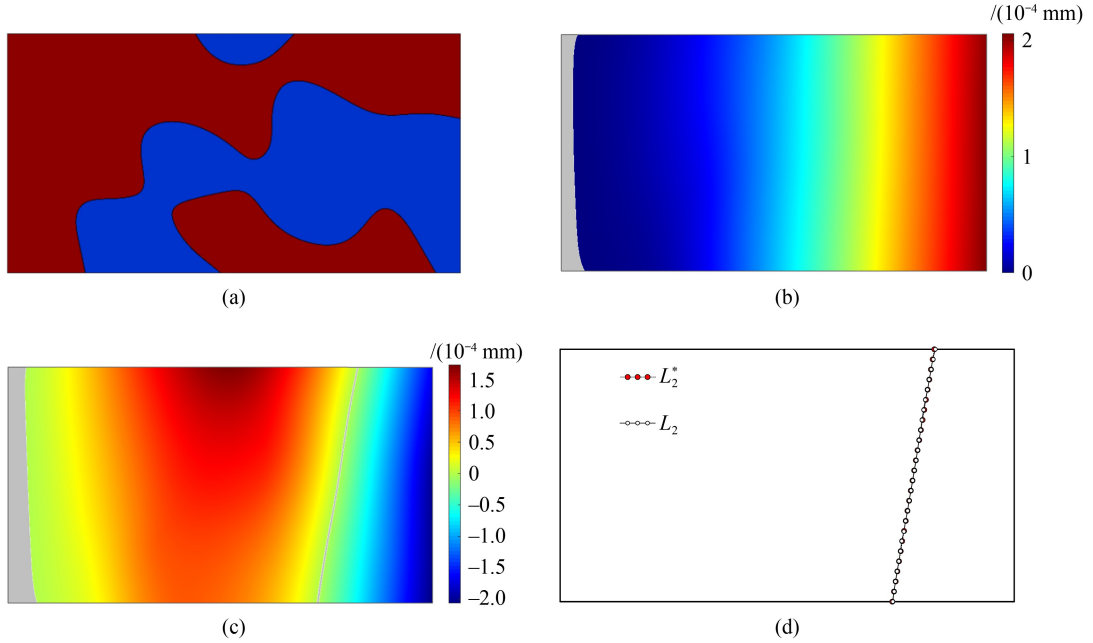


Fig. 6 Optimized solution for achieving the second desired nodal line in Case 2: (a) structural topology, (b) contour for the first-order eigenmode with $\omega_1^* = 15.00$ Hz, (c) contour for the third-order eigenmode, and (d) comparison between the desired nodal line L_2^* and the optimized nodal line L_2 of the third-order eigenmode.

Eq. (4), the objective function is extended as $\min C = \ln \left(\min \left\{ \sum_{m_i=1}^M \sum_{m_j=1}^M (f_{m_i} + f_{m_j}) \right\} \right) - (1 - \alpha) \omega_1$. Notably, two nodal lines of two different eigenmodes are considered here. The m_i and m_j order modes correspond to L_1^* and L_2^* , respectively, and the weighting factor $\alpha = 0.8$. The optimized structure is shown in Fig. 7(a), and the eigenmode contours are presented in Figs. 7(b) and 7(c). The designed nodal lines L_1 and L_2 belong to the second- and third-order eigenmodes, respectively. As shown in Fig. 7(d), L_1 and L_2 are extremely close to the desired nodal lines L_1^* and L_2^* . The maximum error between the optimized and desired nodal lines is 1.217 mm. For the optimized bi-material plate structure, the first-order eigenfrequency is $\omega_1 = 14.53$ Hz.

Table 1 presents the comparison of the results of the cantilever plate optimization in three aforementioned cases. Evidently, compared with the single eigenmode requirement (in Cases 1 and 2), the optimized structure with multiple eigenmode requirements in Case 3 obtains lower first-order eigenfrequency value and the corresponding nodal lines have slightly larger position errors from the desired ones. Notably, the relative position error of nodal lines is still small compared with the whole size of the plate structure. For Case 2, the first-order eigenfrequency of the optimized structure is strictly controlled at the desired value, and the optimized nodal line is also extremely close to the desired one. The above examples demonstrate that the proposed framework is capable of generating meaningful topologies and exhibits a strong ability to control nodal lines and frequencies.

5.2 Nodal line optimization of a piezoelectric vibrator

In this example, we optimize a 3D piezoelectric vibrator that considers the design requirements of eigenmode nodal lines and frequencies. The piezoelectric vibrator is the vibrator structure of a bidirectional linear ultrasonic motor [52–54]. As shown in Fig. 8(a), the vibrator consists of a plate-shaped stator, eight driving gears with the same spacing, and fixed ends for clamping on both sides. The structure is made of titanium alloy with Young's modulus $E_0 = 110$ GPa, Poisson's ratio $\mu = 0.34$, and mass density $\rho_0 = 4500$ kg/m³. With the resonant action of the stator and the piezoelectric ceramic attached to its bottom, the forward or backward motion is formed by the specific positional relationship between the position of the driving gears and the nodal lines of the resonance modes, realizing bidirectional driving capability. The seventh- and eighth-order flexural eigenmodes, called “B7-mode” and “B8-mode” as shown in Figs. 8(b) and 8(c), are utilized as the working modes of this motor. For example, when the B7-mode is excited, all the gears are on the left of the adjacent nodal lines, and the particles on the surface of the gears will produce a right diagonal motion, making the vibrator move forward to the right. Conversely, the B8-mode is the backward mode for left movement.

The relationship between the driving gears and the working modes, particularly the relative position to the nodal lines, plays a decisive role in bidirectional driving capability. The eight driving gears are fixed to the stator, and thus, all the nodal lines for the B7-mode must be on

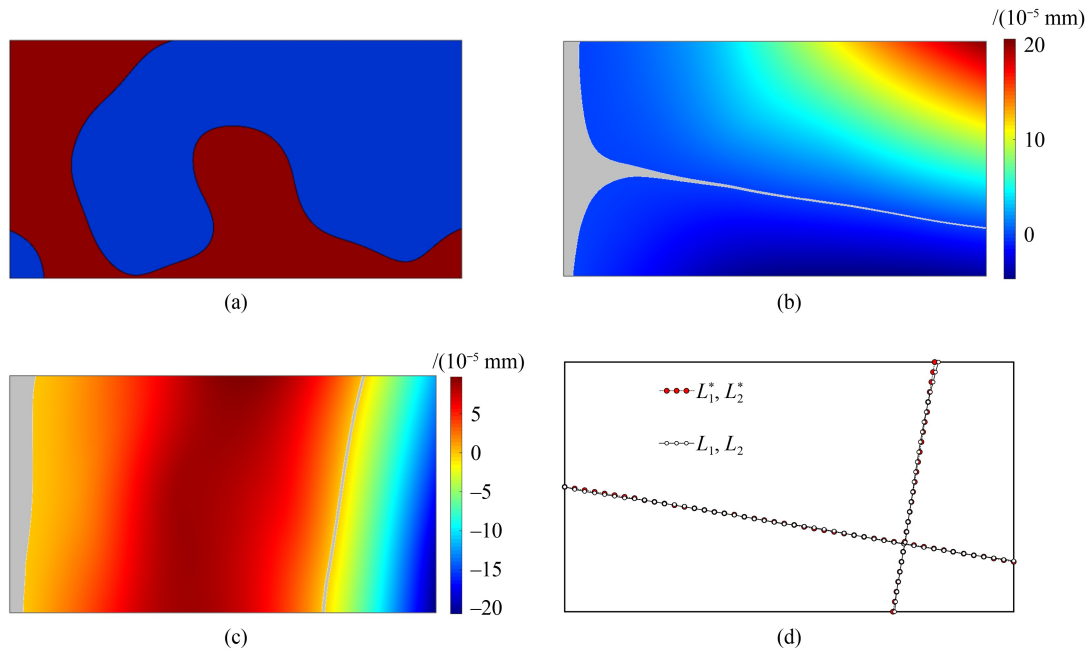
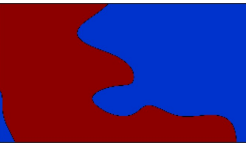
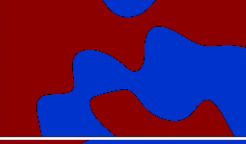
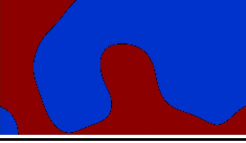


Fig. 7 Optimized solution for achieving two desired nodal lines in Case 3: (a) structural topology, (b) contour for the second-order eigenmode, (c) contour for the third-order eigenmode, and (d) comparison between the optimized and desired nodal lines.

Table 1 Nodal line optimization details of the cantilever plate that considers different design cases

Optimized topology	Maximum error between L_1^* and L_1/mm	Average error between L_1^* and L_1/mm	Maximum error between L_2^* and L_2/mm	Average error between L_2^* and L_2/mm	First-order eigenfrequency/Hz
	0.522	0.162	—	—	21.52
	—	—	0.317	0.121	15.00
	1.082	1.217	1.217	0.323	14.53

the left half of the area between two adjacent driving gears (the eighth gear is not considered at this time). Correspondingly, the right half is for the B8-mode. In Figs. 8(b) and 8(c), the light green regions in the modal deformation diagrams are where the current nodal lines are located, while the red and blue solid line segments are the desired nodal line ranges for the B7-mode and B8-mode, respectively. Setting the left end of the structure as the coordinate origin, the X -coordinates of the desired nodal line range with two decimal places are provided in Table 2. For the initial design of the structure, the B7-mode is the 16th-order eigenmode, and its corresponding resonant frequency (i.e., eigenfrequency) is $\omega_{16} = 273.7$ kHz. The B8-mode is the 18th-order eigenmode

with a frequency of $\omega_{18} = 345.89$ kHz. The initial design satisfies the desired requirement for the nodal lines of B7- and B8-mode. However, the resonant frequencies of these working modes are too high to be achieved easily. Therefore, the optimization model 2 in Eq. (5) is adopted in this optimization problem: for the working modes (B7- and B8-mode), minimizing their corresponding resonant frequencies while keeping the positions of all the nodal lines within the specified range.

The optimization problem must consider the position constraints for 13 nodal lines (6 nodal lines for B7-mode and 7 nodal lines for B8-mode). Considering that these nodal lines for flexural modes can be approximated as straight lines in the longitudinal direction, we select the

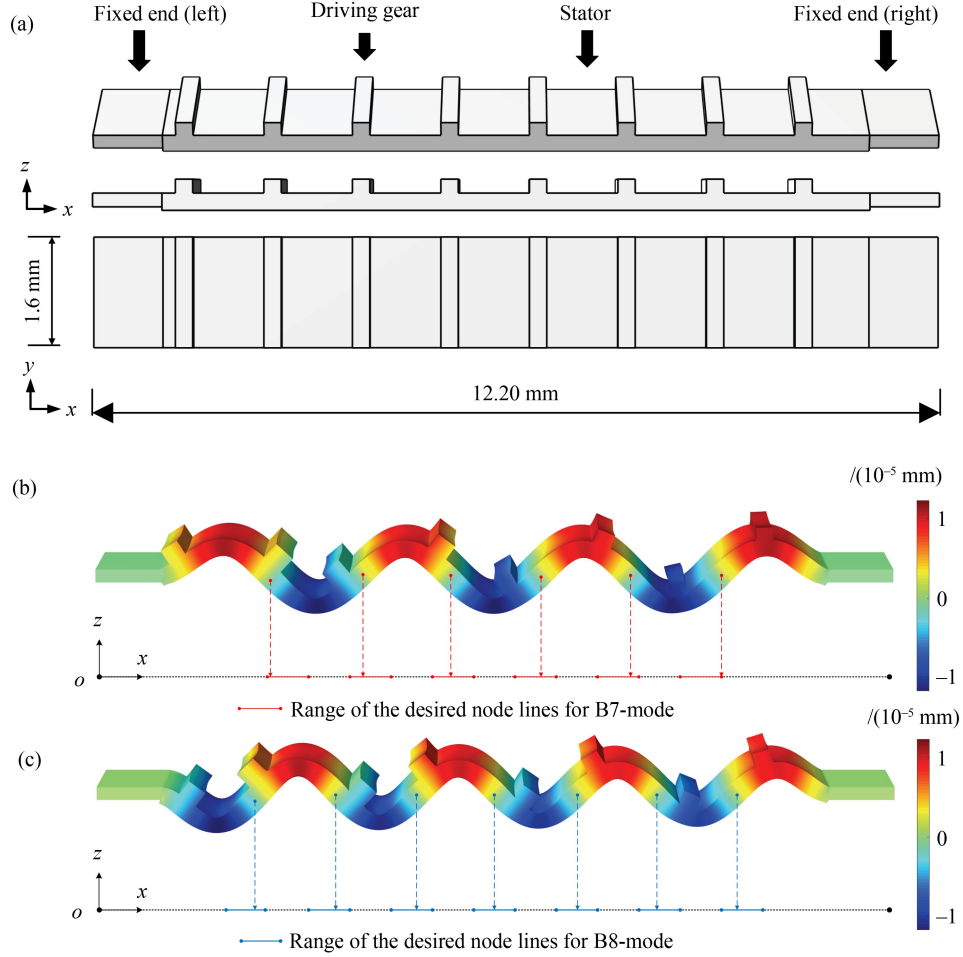


Fig. 8 Schematic of the piezoelectric vibrator and its working modes. (a) Initial design and its front and vertical views. The thickness of the two fixed ends is 0.2 mm, and that of the stator is 0.25 mm. (b) B7-mode contour of the initial design and the positions of the current nodal lines and (c) B8-mode contour of the initial design and the positions of the current nodal lines.

Table 2 Ranges of the desired nodal lines of B7-mode and B8-mode

Working mode	Range of each desired node lines (X coordinate)/mm						
	No. 1	No. 2	No. 3	No. 4	No. 5	No. 6	No. 7
B7-mode	[2.59, 3.23]	[3.87, 4.51]	[5.14, 5.78]	[6.42, 7.06]	[7.69, 8.33]	[8.97, 9.61]	–
B8-mode	[1.96, 2.59]	[3.23, 3.87]	[4.51, 5.14]	[5.78, 6.42]	[7.06, 7.69]	[8.33, 8.97]	[9.61, 10.24]

middle surface (X - Z plane with $Y = 0.8$ mm) as the reference surface to prevent the optimization problem from becoming too complicated, and then use each node on it to represent the node line to which the node belongs. In the two working modes, the midpoints of the ranges of desired nodal lines are regarded as the desired nodes, and the maximum allowable deviation in Eq. (4) is half the horizontal length of those areas ($\Delta_j = 0.31875$ mm, ($j = 1, 2, \dots, 13$)). The first 20 eigenfrequencies and eigenmodes are considered in the optimization problem (i.e., $M = 20$). On the basis of optimization model 2 in Eq. (6), the topology optimization problem of the piezoelectric vibrator, including the nodal line constraints, is reformulated as

$$\min_{\chi(r)} C = \alpha \omega_{B7^*} + (1 - \alpha) \omega_{B8^*},$$

$$\text{s.t. } G = \min \left\{ \sum_{m_{B7}=1}^M \sum_{m_{B8}=1}^M (g_{m_{B7}} + g_{m_{B8}}) \right\} \leq 0,$$

where the weight factors $\alpha = 0.5$. The eigenfrequencies ω_{B7^*} and ω_{B8^*} correspond to the current m_{B7} and m_{B8} order modes with the nodal lines closest to the desired ones, and their orders are determined from the optimization

$$\text{problem } \min \left\{ \sum_{m_{B7}=1}^M \sum_{m_{B8}=1}^M (g_{m_{B7}} + g_{m_{B8}}) \right\}.$$

For this problem, we choose the area between the first and eighth drive gears on the stator plate as the design domain, and it is divided into seven sub-domains by the

fixed driving gears (the light blue regions in Fig. 9). Considering the placement of piezoelectric ceramics, a thickness of 0.1 mm is reserved, and the size of each design sub-domain is all $1.025 \text{ mm} \times 1.6 \text{ mm} \times 0.15 \text{ mm}$. We consider two design options. In periodical Design 1, the design domain can be periodically arranged from a single sub-domain. The seven sub-domains can adopt the same structural design. In aperiodic Design 2, the area between the first and eighth driving gears is considered a whole design domain. The areas where the driving gears are located are the non-design domain. Finite element analysis during optimization is performed using the commercial software COMSOL.

5.2.1 Topological design that considers the periodical design domain

For the optimization design that considers periodical Design 1, only one-half of the sub-design domain with size $1.025 \text{ mm} \times 0.8 \text{ mm}$ is discretized into 80×60 observation points and 80×60 rectangular finite elements, because of the periodicity and symmetry around the reference surface. The correlation length of the material field is set as $l_c = 0.8 \times 0.2 = 0.16 \text{ mm}$. After truncation, 61 design variables are involved in the MFSE-based optimization problem.

The optimized results are presented in Fig. 10. In

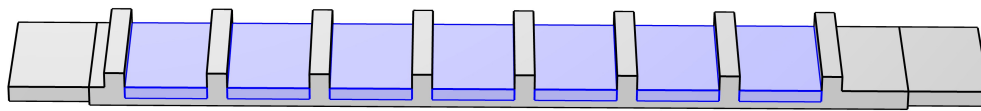


Fig. 9 Diagram of the seven design sub-domains divided by driving gears.

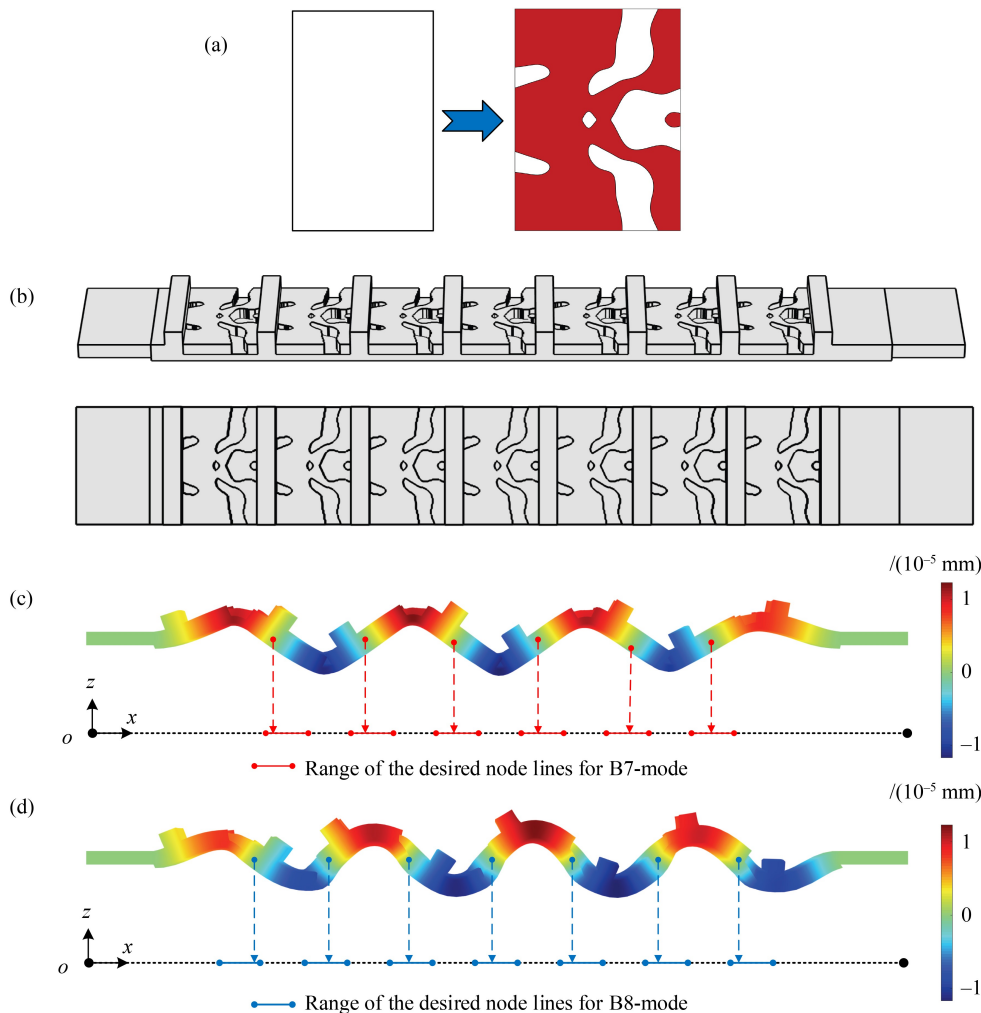


Fig. 10 Optimized results for Design 1: (a) design domain and optimized 2D material distribution, (b) 3D diagram of the optimized structure and its top view, front view of (c) the B7-mode and (d) B8-mode contours for Design 1.

Fig. 10(a), the left side is regarded as the periodic initial design sub-domain, while the final design on the right provides the optimized material distribution of each sub-domain on the X - Y plane, where the red region represents the retained solid material and the white region is the void. The corresponding whole structure is shown in Fig. 10(b). The optimized B7-mode and B8-mode correspond to the 13th- and 19th-order eigenmodes, respectively. Compared with the initial design, the resonant frequencies of the optimized design are reduced from $\omega_{16} = 273.7$ kHz (B7-mode) and $\omega_{18} = 345.89$ kHz (B8-mode) to $\omega_{13} = 186.59$ kHz (B7-mode) and $\omega_{19} = 299.1$ kHz (B8-mode). Their modal deformation diagrams and the positions of the nodal lines are presented in Figs. 10(c) and 10(d). The exact positions of the nodal lines are provided in Table 3. Combined with Table 2 and Fig. 10, all the nodal lines of Design 1 in both working modes are clearly within the desired range.

5.2.2 Topological design that considers the aperiodic design domain

Considering the aperiodic Design 2, the design domain has dimensions of $8.675 \text{ mm} \times 1.6 \text{ mm}$ and contains six $0.25 \text{ mm} \times 1.6 \text{ mm}$ rectangular non-design solid regions. Given the symmetry, only one-half of the design domain, including the non-design domain, as shown in Fig. 11(a), is discretized into 347×32 observation points and 694×64 square elements. We focus on the distribution of materials in the X direction, and thus, the correlation lengths of the material field are set as $l_{cx} = 8.675 \times 0.05 =$

Table 3 Positions of nodal lines for Design 1

Working mode	Positions of each nodal line (X coordinate)/mm						
	No. 1	No. 2	No. 3	No. 4	No. 5	No. 6	No. 7
B7-mode	2.7405	4.0524	5.3583	6.6722	7.9908	9.3004	–
B8-mode	2.4936	3.6453	4.8363	6.0613	7.2775	8.4829	9.6792

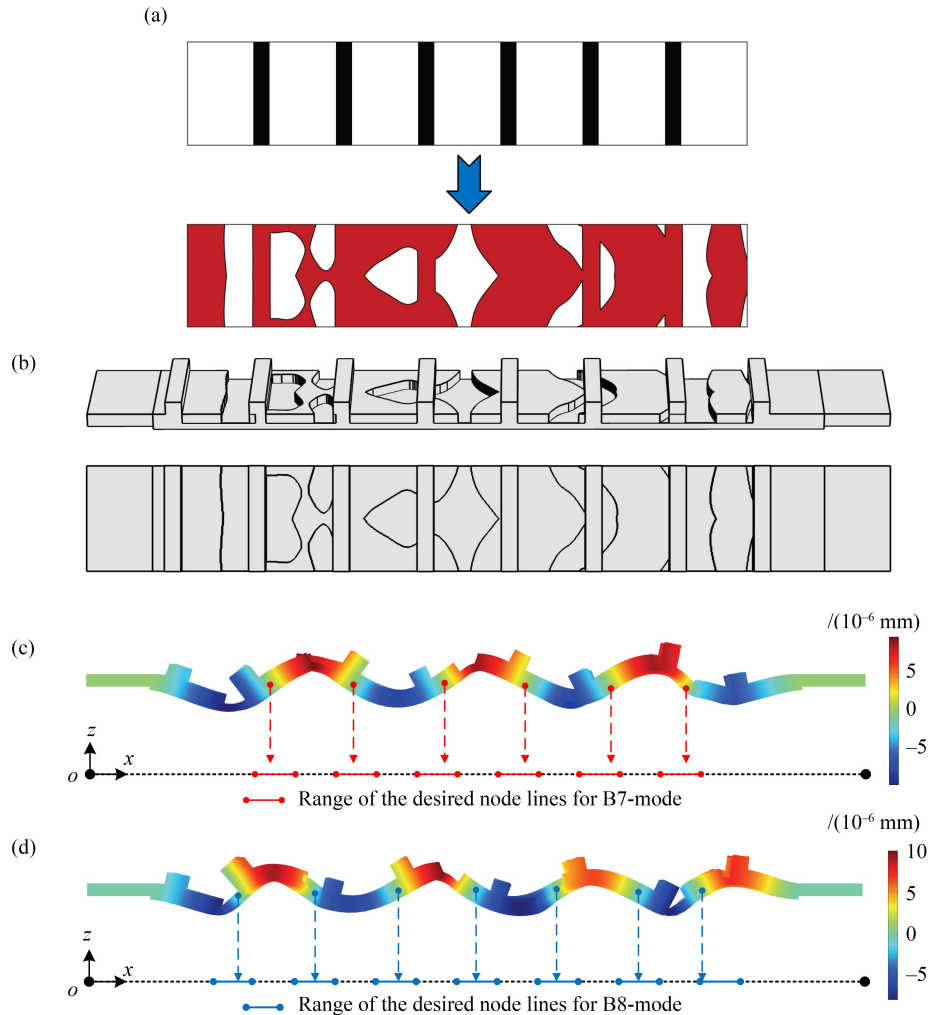


Fig. 11 Optimized results for Design 2: (a) design domain and optimized 2D material distribution, (b) 3D diagram of the optimized structure and its top view, front view of (c) the B7-mode and (d) B8-mode contours for Design 2.

0.43375 mm and $l_{cy} = 0.8 \times 1 = 0.8$ mm, and then, 84 design variables are involved.

The optimized results for Design 2 are presented in Fig. 11. As shown in Figs. 11(a) and 11(b), the material distribution changes are mostly in the X direction as expected. The optimized B7-mode and B8-mode correspond to the 14th- and 17th-order eigenmodes, and the resonant frequencies are reduced from $\omega_{16} = 273.7$ kHz and $\omega_{18} = 345.89$ kHz in the initial design to $\omega_{14} = 191.11$ kHz and $\omega_{17} = 234.35$ kHz in the optimized design. Compared with the optimized results of Design 1, although the resonant frequency of the B7-mode slightly increases, the resonant frequency of the B8-mode exhibits a more evident decrease due to the wider solution space after the periodicity limitation is lifted. In addition, we focus on lateral material distribution, and thus, Design 2 exhibits better performance in terms of manufacturability than Design 1.

The mode shapes and positions of the nodal lines are shown in Figs. 11(c) and 11(d), and the exact locations are provided in Table 4. Combining Table 2 and Figs. 10 and 11, the rightmost nodal line of B8-mode is the most deviated from the midpoint of the desired range in Designs 1 and 2; however, it is still within the desired range. Evidently, the 13 nodal lines of Design 2 also satisfy the required position constraint.

Table 4 Positions of nodal lines in Design 2

Working mode	Positions of each nodal line (X coordinate)/mm						
	No. 1	No. 2	No. 3	No. 4	No. 5	No. 6	No. 7
B7-mode	2.7388	3.9934	5.3497	6.6573	8.0221	9.3377	–
B8-mode	2.4702	3.5546	4.8444	6.0514	7.3277	8.5369	9.6247

The comparison of the two designs with the initial design is presented in Table 5. The resonant frequencies of the two optimized structures are clearly significantly reduced, particularly the B8-mode of Design 2, whose resonant frequency is reduced by 32.25%. During optimization, although the orders of the working modes are all switched, all the corresponding multiple nodal lines satisfy the position constraints, realizing the function of the bi-directional driving of the piezoelectric motor. The optimization example of the piezoelectric vibrator further demonstrates the effectiveness of the proposed framework.

Table 5 Comparison of different designs for the piezoelectric vibrator

Case	B7-mode order and frequency/kHz	Position constraint for B7-mode/mm	B8-mode order and frequency/kHz	Position constraint for B8-mode/mm
Initial design	$\omega_{16} = 273.7$	$g_{16} = 0$	$\omega_{18} = 345.89$	$g_{18} = 0$
Design 1	$\omega_{13} = 186.59$	$g_{13} = 0$	$\omega_{19} = 299.1$	$g_{19} = 0$
Design 2	$\omega_{14} = 191.11$	$g_{14} = 0$	$\omega_{17} = 234.35$	$g_{17} = 0$

6 Conclusions

In this study, a general gradient-free topology optimization framework is proposed to solve the optimization problem of vibrating structures that considers nodal lines and frequencies. Given that no sensitivity is required, the proposed framework inherently avoids various numerical difficulties. For structures in which nodal lines can be explicitly extracted and expressed, numerical applications demonstrate that this framework performs well to obtain the desired nodal lines while satisfying frequency requirements. Although modal switching occurs during optimization, the optimized structural designs still satisfy the requirements.

In the examples of nodal lines and frequency control, the proposed optimization model and gradient-free framework for the bi-material cantilever plate performs well in controlling nodal lines in single-modal and multimodal models. The optimized nodal lines are extremely close to the desired ones while reaching the optimization objective of maximizing the fundamental frequency or obtaining a specific fundamental frequency. For the optimization problem of a piezoelectric vibrator, two design schemes are involved. After optimization, the multiple nodal lines for the multiple working modes are completely in the required position range, and the corresponding eigenfrequencies are considerably reduced, and thus, using the resonance characteristics is more convenient. The examples demonstrate that the proposed framework can accurately control nodal lines and frequencies, exhibiting high potential in the field of dynamic engineering design.

Nomenclature

$\ \cdot\ _2$	2-norm
C	Correlation matrix
$C_d(\mathbf{r})$	Vector $\{C(\mathbf{r}, \mathbf{r}_1), C(\mathbf{r}, \mathbf{r}_2), \dots, C(\mathbf{r}, \mathbf{r}_{N_{\text{MPP}}})\}^T$
E	Young's modulus
E_0	Young's modulus of the considered solid material
E_{\min}	Small values of Young's modulus for avoiding single-element matrices
f_{m_q}	Nodal line measurement function
g_{m_q}	Constraint function
K'	Number of current nodal lines
\mathbf{K}	Structural stiffness matrix
l_c	Given correlation length
$L_1^*, L_2^*, \dots, L_K^*$	Desired nodal lines
L_{k,m_q}	Current nodal line
L_m	Corresponding nodal lines
\mathbf{M}	Mass matrix

N_{MFP}	Number of material points
p	Penalty parameter
\mathbf{r}	Coordinate vector
\mathbf{r}_i	Material points
$\mathbf{r}_{k,j}^*$	Desired node
\mathbf{r}_{k,j,m_q}	Current node
$\mathbf{u}, \ddot{\mathbf{u}}$	Vectors of the degrees of freedom and accelerations, respectively
α	Weighting factor
β	Parameter that controls the smoothness of the mapping
ρ	Mass density
ρ_0	Mass density of the considered solid material
ρ_{\min}	Small values of mass density for avoiding single-element matrices
$\boldsymbol{\eta}$	Vector of the undetermined coefficients or design variables
μ_1, μ_2	Poisson's ratios
λ_m	m th eigenvalue
ω_m	m th eigenfrequency
$\varphi(\mathbf{r})$	Continuous material-field function
Φ	Corresponding eigenvectors
Φ_m	Corresponding eigenmode
$\chi(\mathbf{r})$	Structural topology
Ω_{des}	Design domain
$\zeta(\omega_i)$	User-specified function for some specific order eigenfrequencies
Δ_j	Allowable deviation of the current nodal lines from the desired nodal lines
Λ	Diagonal matrix composed of the first N largest eigenvalues

Acknowledgements This work was supported financially by the Guangdong Basic and Applied Basic Research Foundation, China (Grant No. 2022A1515240059), the National Natural Science Foundation of China (Grant No. 52275237), and the Shenzhen Stability Support Key Program in Colleges and Universities of China (Grant No. GXWD202208171333 29001).

Conflict of Interest The authors declare that they have no conflict of interest.

References

- Grandhi R. Structural optimization with frequency constraints—a review. *AIAA Journal*, 1993, 31(12): 2296–2303
- Zhu J H, Zhang W H, Xia L. Topology optimization in aircraft and aerospace structures design. *Archives of Computational Methods in Engineering*, 2016, 23(4): 595–622
- Rubio W M, Silva E C N, Paulino G H. Toward optimal design of piezoelectric transducers based on multifunctional and smoothly graded hybrid material systems. *Journal of Intelligent Material Systems and Structures*, 2009, 20(14): 1725–1746
- Sanchez-Rojas J L, Hernando J, Donoso A, Bellido J C, Manzaneque T, Ababneh A, Seidel H, Schmid U. Modal optimization and filtering in piezoelectric microplate resonators. *Journal of Micromechanics and Microengineering*, 2010, 20(5): 055027
- Yu Y, Jang I G, Kim I K, Kwak B M. Nodal line optimization and its application to violin top plate design. *Journal of Sound and Vibration*, 2010, 329(22): 4785–4796
- Bendsøe M P, Kikuchi N. Generating optimal topologies in structural design using a homogenization method. *Computer Methods in Applied Mechanics and Engineering*, 1988, 71(2): 197–224
- Bendsøe M P. Optimal shape design as a material distribution problem. *Structural Optimization*, 1989, 1(4): 193–202
- Bendsøe M P, Sigmund O. Material interpolation schemes in topology optimization. *Archive of Applied Mechanics*, 1999, 69(9–10): 635–654
- Xie Y M, Steven G P. A simple evolutionary procedure for structural optimization. *Computers & Structures*, 1993, 49(5): 885–896
- Querín O M, Steven G P, Xie Y M. Evolutionary structural optimization (ESO) using a bidirectional algorithm. *Engineering Computations*, 1998, 15(8): 1031–1048
- Wang M Y, Wang X M, Guo D M. A level set method for structural topology optimization. *Computer Methods in Applied Mechanics and Engineering*, 2003, 192(1–2): 227–246
- Allaire G, Jouve F, Toader A M. Structural optimization using sensitivity analysis and a level-set method. *Journal of Computational Physics*, 2004, 194(1): 363–393
- Takezawa A, Nishiwaki S, Kitamura M. Shape and topology optimization based on the phase field method and sensitivity analysis. *Journal of Computational Physics*, 2010, 229(7): 2697–2718
- Díaz A R, Kikuchi N. Solutions to shape and topology eigenvalue optimization problems using a homogenization method. *International Journal for Numerical Methods in Engineering*, 1992, 35(7): 1487–1502
- Pedersen N L. Maximization of eigenvalues using topology optimization. *Structural and Multidisciplinary Optimization*, 2000, 20(1): 2–11
- Allaire G, Aubry S, Jouve F. Eigenfrequency optimization in optimal design. *Computer Methods in Applied Mechanics and Engineering*, 2001, 190(28): 3565–3579
- Du J B, Olhoff N. Topology optimization of continuum structures with respect to simple and multiple eigenfrequencies. In: *Proceedings of the 6th World Congresses of Structural and Multidisciplinary Optimization*. Rio de Janeiro: International Society for Structural and Multidisciplinary Optimization, 2005
- Ma Z D, Cheng H C, Kikuchi N. Structural design for obtaining desired eigenfrequencies by using the topology and shape optimization method. *Computing Systems in Engineering*, 1994, 5(1): 77–89
- Yoon G H. Structural topology optimization for frequency response problem using model reduction schemes. *Computer Methods in Applied Mechanics and Engineering*, 2010, 199(25–28): 1744–1763

20. Ma Z D, Kikuchi N, Cheng H C. Topology design for vibrating structures. *Computer Methods in Applied Mechanics and Engineering*, 1995, 121(1–4): 259–280
21. Zhang X P, Kang Z. Dynamic topology optimization of piezoelectric structures with active control for reducing transient response. *Computer Methods in Applied Mechanics and Engineering*, 2014, 281: 200–219
22. Takezawa A, Daifuku M, Nakano Y, Nakagawa K, Yamamoto T, Kitamura M. Topology optimization of damping material for reducing resonance response based on complex dynamic compliance. *Journal of Sound and Vibration*, 2016, 365: 230–243
23. Jensen J S, Pedersen N L. On maximal eigenfrequency separation in two-material structures: the 1D and 2D scalar cases. *Journal of Sound and Vibration*, 2006, 289(4–5): 967–986
24. Du J B, Olhoff N. Topological design of freely vibrating continuum structures for maximum values of simple and multiple eigenfrequencies and frequency gaps. *Structural and Multidisciplinary Optimization*, 2007, 34(2): 91–110
25. Liu P, Zhang X P, Luo Y J. Topological design of freely vibrating bi-material structures to achieve the maximum band gap centering at a specified frequency. *Journal of Applied Mechanics*, 2021, 88(8): 081003
26. Tcherniak D. Topology optimization of resonating structures using SIMP method. *International Journal for Numerical Methods in Engineering*, 2002, 54(11): 1605–1622
27. Nishiwaki S, Maeda Y, Izui K, Yoshimura M, Matsui K, Terada K. Topology optimization of mechanical structures targeting vibration characteristics. *Journal of Environmental and Engineering*, 2007, 2(3): 480–492
28. Maeda Y, Nishiwaki S, Izui K, Yoshimura M, Matsui K, Terada K. Structural topology optimization of vibrating structures with specified eigenfrequencies and eigenmode shapes. *International Journal for Numerical Methods in Engineering*, 2006, 67(5): 597–628
29. Tsai T D, Cheng C C. Structural design for desired eigenfrequencies and mode shapes using topology optimization. *Structural and Multidisciplinary Optimization*, 2013, 47(5): 673–686
30. Xue L, Wen G L, Wang H X, Liu J. Eigenvectors-guided topology optimization to control the mode shape and suppress the vibration of the multi-material plate. *Computer Methods in Applied Mechanics and Engineering*, 2022, 391: 114560
31. Nakasone P H, Silva E C N. Dynamic design of piezoelectric laminated sensors and actuators using topology optimization. *Journal of Intelligent Material Systems and Structures*, 2010, 21(16): 1627–1652
32. Rubio W M, Silva E C N, Paulino G H. Toward optimal design of piezoelectric transducers based on multifunctional and smoothly graded hybrid material systems. *Journal of Intelligent Material Systems and Structures*, 2009, 20(14): 1725–1746
33. Rubio W M, Paulino G H, Silva E C N. Tailoring vibration mode shapes using topology optimization and functionally graded material concepts. *Smart Materials and Structures*, 2011, 20(2): 025009
34. Giannini D, Braghin F, Aage N. Topology optimization of 2D in-plane single mass MEMS gyroscopes. *Structural and Multidisciplinary Optimization*, 2020, 62(4): 2069–2089
35. Giannini D, Aage N, Braghin F. Topology optimization of MEMS resonators with target eigenfrequencies and modes. *European Journal of Mechanics—A/Solids*, 2022, 91: 104352
36. Xiang J W, Zhang C L, Zhou C R, Zhang A Z. Structural dynamics optimum design with given frequencies and position of mode shape node lines. *Chinese Journal of Computational Mechanics*, 1995, 4: 401–408 (in Chinese)
37. Chen H, Zhou C. Structural design subjected to multiple frequencies positions of nodal lines and other constraints. *Chinese Journal of Applied Mechanics*, 1996, 1: 59–63 (in Chinese)
38. Liu Z X, Qian Y J, Yang X D, Zhang W. Panel flutter mechanism of rectangular solar sails based on travelling mode analysis. *Aerospace Science and Technology*, 2021, 118: 107015
39. Gong D, Zhou J S, Sun W J, Sun Y, Xia Z H. Method of multi-mode vibration control for the carbody of high-speed electric multiple unit trains. *Journal of Sound and Vibration*, 2017, 409: 94–111
40. Li F, Wang J, Shi H, Wu P. Research on causes and countermeasures of abnormal flexible vibration of car body for electric multiple units. *Journal of Mechanical Engineering*, 2019, 55(12): 178–188 (in Chinese)
41. Mao Z Y, Chen G P, He H. Evolutionary optimization design of the structural dynamic characteristics under multi constraints. *Applied Mechanics and Materials*, 2010, 29–32: 906–911 (in Chinese)
42. Kim T S, Kim Y Y. Mac-based mode-tracking in structural topology optimization. *Computers & Structures*, 2000, 74(3): 375–383
43. Luo Y J, Xing J, Kang Z. Topology optimization using material-field series expansion and kriging-based algorithm: an effective non-gradient method. *Computer Methods in Applied Mechanics and Engineering*, 2020, 364: 112966
44. Zhang X P, Luo Y J, Yan Y, Liu P, Kang Z. Photonic band gap material topological design at specified target frequency. *Advanced Theory and Simulations*, 2021, 4(10): 2100125
45. Yan Y, Liu P, Zhang X P, Luo Y J. Photonic crystal topological design for polarized and polarization-independent band gaps by gradient-free topology optimization. *Optics Express*, 2021, 29(16): 24861–24883
46. Zhang X P, Xing J, Liu P, Luo Y J, Kang Z. Realization of full and directional band gap design by non-gradient topology optimization in acoustic metamaterials. *Extreme Mechanics Letters*, 2021, 42: 101126
47. Luo Y J, Bao J W. A material-field series-expansion method for topology optimization of continuum structures. *Computers & Structures*, 2019, 225: 106122
48. Kreisselmeier G, Steinhauser R. Systematic control design by optimizing a vector performance index. *IFAC Proceedings Volumes*, 1980, 12(7): 113–117
49. He J J, Kang Z. Achieving directional propagation of elastic waves via topology optimization. *Ultrasonics*, 2018, 82: 1–10
50. Stolpe M, Svanberg K. An alternative interpolation scheme for minimum compliance topology optimization. *Structural and Multidisciplinary Optimization*, 2001, 22(2): 116–124
51. Luo Y J, Zhan J J, Xing J, Kang Z. Non-probabilistic uncertainty

- quantification and response analysis of structures with a bounded field model. *Computer Methods in Applied Mechanics and Engineering*, 2019, 347: 663–678
52. Su H L, Zhao X D, Zhao C S. Study on moving mechanism of a rotatory type standing wave ultrasonic motor with single phase driver. *Piezoelectric & Acoustooptic*, 2001, 23(4): 306–308,312
53. Qian X H, Shen M H. A new standing-wave linear moving ultrasonic motor based on two bending modes. *Applied Mechanics and Materials*, 2011, 101–102: 140–143
54. Liu Z, Wang H, Yang P, Dong Z Y, Zhang L H. Dynamic modeling and analysis of bundled linear ultrasonic motors with non-ideal driving. *Ultrasonics*, 2022, 124: 106717